Medical Image Analysis 14 (2010) 149–159

Contents lists available at ScienceDirect

Medical Image Analysis

journal homepage: www.elsevier.com/locate/media

Automated detection of intracranial aneurysms based on parent vessel 3D analysis

Alexandra Lauric [a,*], Eric Miller [a,b], Sarah Frisken [a], Adel M. Malek [c,d]

[a] Tufts University, Department of Computer Science, 161 College Ave, Medford, MA 02155, United States
[b] Tufts University, Department of Electrical and Computer Engineering, 161 College Ave, Medford, MA 02155, United States
[c] Tufts University School of Medicine, 145 Harrison Ave, Boston, MA 02111, United States
[d] Tufts Medical Center, Department of Neurosurgery, 800 Washington St., Boston, MA 02111, United States

ARTICLE INFO

Article history:
Received 8 December 2008
Received in revised form 20 October 2009
Accepted 29 October 2009
Available online 11 November 2009

Keywords:
Intracranial aneurysms
Aneurysm detection
Computed-aided diagnostic
Surface descriptor
Writhe number

ABSTRACT

The detection of brain aneurysms plays a key role in reducing the incidence of intracranial subarachnoid hemorrhage (SAH) which carries a high rate of morbidity and mortality. The majority of non-traumatic SAH cases is caused by ruptured intracranial aneurysms and accurate detection can decrease a significant proportion of misdiagnosed cases. A scheme for automated detection of intracranial aneurysms is proposed in this study. Applied to the segmented cerebral vasculature, the method detects aneurysms as suspect regions on the vascular tree, and is designed to assist diagnosticians with their interpretations and thus reduce missed detections. In the current approach, the vessels are segmented and their medial axis is computed. Small regions along the vessels are inspected and the writhe number is introduced as a new surface descriptor to quantify how closely any given region approximates a tubular structure. Aneurysms are detected as non-tubular regions of the vascular tree. The geometric assumptions underlying the approach are investigated analytically and validated experimentally. The method is tested on 3D-rotational angiography (3D-RA) and computed tomography angiography (CTA). In our experiments, 100% sensitivity was achieved with average false positives rates of 0.66 per study on 3D-RA data and 5.36 false positive rates per study on CTA data.

© 2009 Elsevier B.V. All rights reserved.

1. Introduction

Subarachnoid hemorrhage (SAH) is a serious cause of stroke which affects 30,000 patients in North America annually. SAH accounts for a quarter of cerebrovascular deaths, with 80% of the non-traumatic SAH cases being caused by a ruptured intracranial aneurysm (Edlow et al., 2008; Wardlaw and White, 2000). An intracranial aneurysm is a localized pathological dilatation of a blood vessel. It is reported that up to 2% of the general population harbors aneurysms (Rinkel et al., 1998; Juvela, 2004). Most of these aneurysms are asymptomatic and remain undetected with only a small proportion proceeding to rupture and consequent SAH, with an annual incidence of approximately 1% (Wardlaw and White, 2000; Johnson et al., 2001). However, in the case of a ruptured aneurysm, the initial bleed is fatal in 10–20% of instances and despite improvements in patient management, the incidence of SAH has not declined over time and the morbidity rate is still reported between 25% and 50% in patients surviving aneurysm ruptures (Wardlaw and White, 2000; Juvela, 2004; Suarez et al., 2006).

Detecting intracranial aneurysms from imaging scans is an essential step in the prevention of aneurysmal SAH and its attendant complications (Wardlaw and White, 2000), as treatment of aneurysms using endovascular or surgical methods carries a lower rate of complication when performed in unruptured versus ruptured aneurysms (Brisman et al., 2006). Although aneurysm detection is currently performed visually by experienced diagnosticians, there is an increasing interest in computed-aided diagnostic (CAD) systems to assist diagnosticians and possibly improve diagnostic accuracy, while limiting missed detection.

The purpose of this work is the introduction and initial proof of concept of a new 3D shape feature, namely the writhe number, used for detecting aneurysms in high quality segmentation of vasculatures. As such our contribution is twofold. First, we concentrate on our theoretical contribution by introducing the writhe number as a new 3D descriptor used to characterize surfaces. Known in curve theory since its introduction by Fuller (1971), the writhe number is used to describe the global geometry of a closed space curve or knot (Agarwal et al., 2004; Berger and Prior, 2006). To the best of our knowledge, this paper represents the first time the writhe number is extended to surfaces. Second, we develop a writhe number-based scheme for the automatic detection of aneurysms and demonstrate its utility via the analysis of both 3D-RA and CTA data.

* Corresponding author. Tel.: +1 7816486819.
E-mail addresses: alauri02@cs.tufts.edu (A. Lauric), elmiller@ecs.tufts.edu (E. Miller), frisken@cs.tufts.edu (S. Frisken), amalek@tuftsmedicalcenter.org (A.M. Malek).

1361-8415/$ - see front matter © 2009 Elsevier B.V. All rights reserved.
doi:10.1016/j.media.2009.10.005

Existing aneurysm detection methods focus on magnetic resonance angiography (MRA) data and are usually two-step processes (Arimura et al., 2004; Uchiyama et al., 2005; Kobashi et al., 2006). First, potential regions of interest (potential aneurysms) are detected by pre-processing the data using dot-enhancement filters (Arimura et al., 2004) and/or by analyzing the geometry of the vessels. Second, false positive reduction methods are applied on the areas highlighted in the first step, where the reduction scheme depends on the specificity of the detection method used in the first step.

The detection method presented here is based on the 3D shape analysis of the vessels and it is performed on the segmented vasculature. We assume that a short segment of a normal vessel can be locally modeled as a tube with a circular cross-section whose medial axis is a line segment or a quadratic (i.e., parabolic) curve. This assumption is validated experimentally on clinical data. Using the writhe number our method identifies aneurysms as regions of the vasculature which are not well modeled as a tube or an extruded parabola. Specifically, regions along the vessels where the writhe number is non-zero are reported as possible aneurysms. The method uses a false positive reduction scheme in which small regions are eliminated from positive results.

In this study, the detection method is tested on 3D-RA and CTA patient data. The work concentrates on the use of a high resolution modality, in this case 3D-RA, to enable the evaluation of the algorithm characteristics without being hampered with the inevitably lower spatial resolution of most current MRA and CTA data. We also consider the application of the algorithm to CTA data and discuss its performance and limitations on this more challenging imaging modality.

Free-response operator characteristic (FROC) analysis is applied to evaluate the performance of the proposed detection system. FROC analysis shows how the sensitivity of the system changes function of the threshold value used to eliminate small positive results. In our experiments, the sensitivity of the aneurysm detection method was found to be 100% with 0.66 false positives per study on ten distinct 3D-RA datasets and 5.36 false positives per study on ten unrelated CTA datasets.

The eventual clinical goal of this research is to offer an added safety net to the diagnostician and the patient, by making available a concordance check protocol that would point the clinician to potential areas of concern that may have been missed by the current method of visual inspection. The added value of such a tool will need to be evaluated by prospective clinical trials.

The paper is structured as follows: existing work in vessel segmentation and aneurysm detection is presented in Section 2. In Section 3 we introduce the writhe number followed by details about the detection method in Section 4. Test data and pre-processing procedures are presented in Section 5. Results are reported in Section 6 and discussed in Section 7, together with directions for future work. Proofs involving the writhe number are demonstrated in Appendix A.

2. Related work

When interpreting scans and searching for aneurysms, it is important for clinicians to have access to the underlying 3D structures from the 2D studies. Because 3D-RA, CTA and MRA data provide vessel and aneurysm positions in cross-sectional images only, the extraction of 3D structures from 2D images is achieved through segmentation. A great deal of research has been carried out in developing algorithms for the segmentation of cerebral vasculature, including aneurysms, from MRA and CTA studies (Fridman et al., 2004; Hernandez and Frangi, 2007; Radaelli and Peiro, 2009). Vessels segmentation remains a challenging task and the research in this field remains active. Refer to Luo and Zhong (2005) for a survey of algorithms for vessel segmentation from MRA data and Kirbas and Quek (2003) for a survey on vessel extraction techniques and algorithms applied to MRA, CTA and 3D-RA datasets.

In order to visually isolate aneurysms from segmented volumes, it is necessary to study the entire vasculature. Small aneurysms are often visible only from specific viewing directions and may go undetected, leading to misdiagnosis. In contrast, CAD-based aneurysm detection methods highlight possible aneurysm areas and may help improve diagnostic accuracy and ultimately, reduce diagnostic times.

Uchiyama et al. (2005) detect potential aneurysms by measuring the degree of convergence of the gradient vectors at each point in the segmented vessels. Analysis of the size, shape and image intensity of each candidate region is performed to eliminate false positive results. Kobashi et al. (2006) construct "normal vasculature models" by dilating the vessels axis obtained from thinning of the segmented vasculature, such that the resulting vasculature model has circular cross-sections. Potential aneurysms are obtained by subtracting the "normal vasculature model" from the segmented arteries. False positive reduction is based on evaluating nine feature values with respect to the shape and intensity of the aneurysms candidates. In the method proposed by Arimura et al. (2004), MRA images are pre-processed using a dot-enhancement filter and potential aneurysms are detected by grey level thresholding of the enhanced images. False positive reduction is performed based on size, local structure and image intensity features. False positive rates are further reduced by finding short branches in the medial axis of the vessels and using that as a high likelihood of small aneurysms (Arimura et al., 2005). A shape-based difference image technique is used to improve the detection method by extracting additional features based on the local changes in vessel thickness, where thin regions have a higher likelihood of being false positives (Arimura et al., 2006). Local changes in vessel thickness are determined based on distance-transformed and skeleton images.

Our work is similar to Kirbas and Quek (2003) in that we evaluate the intracranial vasculature as a whole and consider normal vessels to be approximated by tubular structures. However, instead of constructing a global vasculature model we focus on the local 3D geometry of the input vessels. Consequently, we are introducing a new surface descriptor, called the writhe number, which is used to study vessels locally and determine if regions along the vasculature can be approximated by tubular structures. As used in this work, the writhe number takes into account the 3D geometry of both the parent vessels and the potential aneurysms and proved to be very accurate in distinguishing between healthy vessels and regions with potential aneurysms.

3. Writhe number

3.1. The writhe of surfaces

The writhe number was introduced by Fuller (1971) and it is used in curve theory to measure how much a curve twists and coils. When a second curve is placed nearly parallel to the first one, the writhe number measures how much the second curve twists about the first (Berger and Prior, 2006). In biomedical engineering, the writhe number is used to study the shape and topology of DNA (Klenin and Langowski, 2000; Rossetto and Maggs, 2003) or to characterize the shape of curves on 3D surfaces, such as the curves of sulci and gyri on the cortical surface (Hurdal et al., 2008). To the best of our knowledge, this paper represents the first time the writhe number is used to characterize surfaces.

We are defining the writhe of surfaces similar to the writhe of curves, except using surface normals rather than curve tangents. Similar to curve theory, the writhe of surface points describe the contribution of a point to the overall complexity of the surface.

Given two points $\mathbf{p}$ and $\mathbf{p}'$ on a surface S, we define a relationship w between them as

$$w(\mathbf{p},\mathbf{p}') = \frac{\left[\hat{\mathbf{n}}_{\mathbf{p}}, \mathbf{p}' - \mathbf{p}, \hat{\mathbf{n}}'_{\mathbf{p}}\right]}{\|\hat{\mathbf{n}}_{\mathbf{p}}\| \cdot \|\mathbf{p}' - \mathbf{p}\| \cdot \|\hat{\mathbf{n}}'_{\mathbf{p}}\|}, \tag{1}$$

where $\hat{\mathbf{n}}_{\mathbf{p}}$ is the surface normal at point $\mathbf{p}$, $\|\cdot p\|$ is the norm of a vector and $[\mathbf{a},\mathbf{b},\mathbf{c}]$ is the triple scalar product of vectors $\mathbf{a}$, $\mathbf{b}$ and $\mathbf{c}$. The triple scalar product is defined as $[\mathbf{a},\mathbf{b},\mathbf{c}] = \mathbf{a} \bullet (\mathbf{b} \times \mathbf{c})$, where $\mathbf{a} \bullet \mathbf{b}$ denotes a dot product and $\mathbf{a} \times \mathbf{b}$ denotes a cross-product. The following identities involving the triple scalar product are also true: $\mathbf{a} \bullet (\mathbf{b} \times \mathbf{c}) = \mathbf{b} \bullet (\mathbf{c} \times \mathbf{a}) = \mathbf{c} \bullet (\mathbf{a} \times \mathbf{b})$.

Note that $w(\mathbf{p},\mathbf{p}') = w(\mathbf{p}',\mathbf{p})$ and $w(\mathbf{p},\mathbf{p}')$ is a pseudoscalar, meaning that it behaves like a scalar but changes sign under inversion. It can be proven using linear algebra that $\mathbf{a} \bullet (\mathbf{b} \times \mathbf{c}) = -(-\mathbf{a}) \bullet ((-\mathbf{b}) \times (-\mathbf{c}))$.

For our processing, we require the notion of a local neighborhood, $N(\mathbf{p})$, about a point $\mathbf{p}$ on the surface of a vessel. Formally, a point $\mathbf{p}'$ belongs to $N(\mathbf{p})$ if and only if the following two conditions are satisfied. First, the geodesic path from $\mathbf{p}$ to $\mathbf{p}'$ belongs to $N(\mathbf{p})$. This condition guarantees that $N(\mathbf{p})$ is connected. Second, $\|\mathbf{p}' - \mathbf{p}\| \leqslant d$, $d \in \mathbb{R}_+$. The Euclidean metric, $\|\cdot\|$, determines the size of the neighborhood. The writhe number of a point $\mathbf{p}$, given its local neighborhood $N(\mathbf{p})$ is a surface integral defined as

$$W(\mathbf{p}, N(\mathbf{p})) = \int_{\mathbf{p}' \in N(\mathbf{p})} w(\mathbf{p},\mathbf{p}')\, dp'. \tag{2}$$

In a discrete space Eq. 2 becomes

$$W(\mathbf{p}, N(\mathbf{p})) = \sum_{\mathbf{p}' \in N(\mathbf{p})} w(\mathbf{p},\mathbf{p}'). \tag{3}$$

3.2. Writhe number analysis

For this work, we assume healthy vessels can be modeled locally as cylinders or extruded parabolas. The assumption is validated experimentally in Section 5.3. The writhe number as defined in Section 3.1 is used to detect perturbations from cylinders and extruded parabolas along the vasculature. We claim that if $N(\mathbf{p})$ is a cylinder or an extruded surface along a parabola then $W(\mathbf{p}, N(\mathbf{p})) = 0$, i.e. the writhe number is zero in regions of normal vasculature. Consequently, regions with non-zero writhe numbers are reported as possible aneurysms. The claim is discussed here and proven in Appendix A, using the pseudoscalar quality of the writhe number.

3.2.1. The writhe of a cylinder

If $N(\mathbf{p})$ is a cylinder, we claim that for every point $\mathbf{p}_1 \in N(\mathbf{p})$ there exists a second point $\mathbf{p}_2 \in N(\mathbf{p})$, such that the Euclidean distance $|\mathbf{p}_1 - \mathbf{p}| = |\mathbf{p}_2 - \mathbf{p}|$ and the line segment $\mathbf{p}_1\mathbf{p}_2$ lie on the cylinder surface (Fig. 1a). The two conditions ensure that the pair $(\mathbf{p}_1, \mathbf{p}_2)$ is unique. It can be proven that $w(\mathbf{p},\mathbf{p}_1) = -w(\mathbf{p},\mathbf{p}_2)$ (Appendix A.1). Pairs of points $(\mathbf{p}_1, \mathbf{p}_2)$ cancel each others in the writhe number summation and $W(\mathbf{p}, N(\mathbf{p})) = 0$.

3.2.2. The writhe of an extruded surface along a parabola

If $N(\mathbf{p})$ is a non-self-intersecting extruded parabola, its medial axis is a parabola. Let $\mathbf{p}$ correspond to the apex of the parabola. For every point $\mathbf{p}_1 \in N(\mathbf{p})$ there exists a second point $\mathbf{p}_2 \in N(\mathbf{p})$, such that the Euclidean distance $\mathbf{p}_1 - \mathbf{p}| = |\mathbf{p}_2 - \mathbf{p}|$ and $\mathbf{p}_1, \mathbf{p}_2$ lie on the extruded surface along a parabola parallel to the medial axis (Fig. 1b). The two conditions ensure that the pair $(\mathbf{p}_1, \mathbf{p}_2)$ is unique.

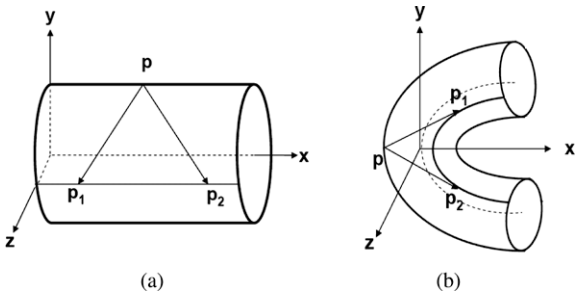


Fig. 1. (a) The writhe number of a cylinder is zero based on the symmetric nature of a cylinder. (b) The writhe number of an extruded parabola is also zero.

It can be proven that $w(\mathbf{p},\mathbf{p}_1) = -w(\mathbf{p},\mathbf{p}_2)$ (Appendix A.2). Pairs of points $(\mathbf{p}_1, \mathbf{p}_2)$ cancel each others in the writhe number summation and $W(\mathbf{p}, N(\mathbf{p})) = 0$.

3.2.3. The writhe number more generally

Intuitively, given a surface N and a point $\mathbf{p} \in N$ on the surface, $w(\mathbf{p}, N) = 0$ if N displays mirror symmetry about a mirror plane which passes through point $\mathbf{p}$ and contains the normal at $\mathbf{p}$. Mirror symmetry occurs when two halves of a whole are each other's mirror images (Hargittai and Hargittai, 1994). Mirror symmetry guarantees that for every point $\mathbf{p}_1 \in N$ there exists a second point $\mathbf{p}_2 \in N$, such that the Euclidean distance $|\mathbf{p}_1 - \mathbf{p}| = |\mathbf{p}_2 - \mathbf{p}|$, with $\mathbf{p}_1$ and $\mathbf{p}_2$ located on different sides of the mirror plane. A cylinder has an infinity of mirror planes passing through its axis. An extruded parabola has two mirror planes, one which contains the medial axis and one perpendicular to the medial axis. While aneurysmal regions may also show some symmetries, in practice most of the points on the surface of aneurysms do not sit on mirror planes and will have non-zero writhe numbers. Section 4.5 provides details on how local neighborhoods are constructed for surface points on both normal vessels and aneurysmal areas. The construction guarantees to take advantage of the differences between normal vessels and aneurysmal regions.

4. Method

4.1. Overview of the detection algorithm

The detection method takes as input a 3D volume in which the cerebral vasculature has been segmented from the background. The medial axis of the vessels is computed from the segmented volume. Similar to Arimura et al. (2005), we consider that aneurysms appear as short branches in the medial axis of the vasculature. Local neighborhoods are determined for surface points along short branches such that they satisfy the connectedness and size conditions described in Section 3.1. The writhe numbers are computed for each local neighborhood and regions with non-zero writhe numbers are reported as possible aneurysms. The size of each region is determined and small regions are eliminated from results based on a thresholding criteria. Details about each of these steps are presented below.

4.2. Segmentation

The detection method requires a segmented volume of the cerebral vasculature. The appropriate segmentation method depends on the modality of the input data (CTA, MRA, 3D-RA). Practical details about the pre-processing and segmentation techniques used on our particular input data are provided in Sections 5. From the segmented volume, the surface of the vessels is described as the set of voxels which have at least one adjacent background voxel.

4.3. Medial axis detection

The medial axis of the vessels is computed applying the method described by Bouix et al. (2005) and using a skeletonization algorithm which exploits the distance field corresponding to the segmented vessels.

4.4. Short branches selection

The aneurysm detection method takes advantage of the fact that aneurysms appear as small branches along the medial axis (Arimura et al., 2005). Once the medial axis is computed, each voxel on the medial axis is labeled as an end point (the voxel has one adjacent neighbor), a connecting point (the voxel has two adjacent neighbors) or a junction point (the voxel has three or more adjacent neighbors). Short branches are paths between end points and junction points having the length smaller than a threshold value where the threshold is set using voxel dimensions to detect aneurysms up to 50 mm long. In studies, 90% of the aneurysms are smaller than 25 mm in diameter and only 10% are giant aneurysms with sizes between 25–50 mm (Rooij and Sluzewski, 2006). It should be noted that most of the short branches determined this way are actually noise on the medial axis and are only few voxels long. However, for our detection algorithm, the medial axis provides vital information about aneurysms locations and while reducing the sensitivity of the medial axis algorithm or smoothing the result might reduce the number of short branches, it could also result in misdetection of small aneurysms.

4.5. Local neighborhood model

Local neighborhoods are determined for the collection of points on the surface of short branches. Given a surface point, **p**, we want to determine its local neighborhood $N(\mathbf{p})$. A second point, **c**, is found such that **c** belongs to the medial axis, **c** is the closest point to **p** and **c** was labeled as a short branch medial point in Section 4.4. In most of the cases, **p** is a point on the surface of normal vessels and **c** is a noise point on the medial axis sitting close to the true medial axis of the region (Fig. 2a and b).

Let R be the Euclidean distance between points **c** and **p**. The local neighborhood of point **p** is built around point **c** and is defined as the connected set of points whose Euclidean distance is within $R\sqrt{2}$ from **c** (Fig. 2). Using this method, the local neighborhood of **p** is a small segment of the vasculature. In the case of a cylinder, the $R\sqrt{2}$ threshold guarantees a one-to-one length-diameter aspect ratio, which works well in practice. Depending on the local bending of the vessels near **p**, the medial axis of $N(\mathbf{p})$ can be approximated by either a line segment and in this case **c** is the midpoint of the segment, or by a parabola in which case **c** is the apex of the parabola (this will be verified experimentally in Section 5.3). For healthy vessels, the construction guarantees that **p** sits on a mirror plane of $N(\mathbf{p})$.

The local neighborhood of a surface point is determined as described above independent of the location of the point on the vasculature. Fig. 2c shows the local neighborhood of a point on the surface of an aneurysm. The neighborhood contains part of the aneurysm as well as a portion of the parent vessel. Because the points on the surface of an aneurysm concentrate around the same medial axis points, they share the same local neighborhood. Even in those cases where the aneurysm area might display some symmetries, most surface points will not sit on mirror planes and will have non-zero writhe numbers. Exceptions might be fusiform aneurysms which present as local dilatations of an artery, having perfectly circular cross-sections and showing symmetries similar to those of normal vessels. In practice, our method was able to detect certain biological fusiform aneurysms because of their uneven dilatations in multiple directions perpendicular to the vessel axis.

4.6. Writhe number computation

For each local neighborhood, the writhe numbers are computed according to Eq. 3. To a very high degree of accuracy, the nominal behavior of the vasculature results in the writhe number being equal to zero for the neighborhoods along healthy vessels. This follows because locally normal vessels are shaped as cylinders or extruded parabolas which in theory have a zero writhe number. The local neighborhoods of points on the aneurysms do not display the same symmetries as cylinders and extruded parabolas and as a result have non-zero writhe numbers.

4.7. False positive reduction

Adjacent voxels on the surface of the vessels having non-zero writhe numbers are clustered in regions which are considered positive results and are highlighted as possible aneurysms. The detection method based on writhe numbers shows high specificity and as a result we are able to threshold positive results using simple features related to the size of the candidate regions. Specifically, our source data originated from multiple modalities, collected with different scanner models, and having different voxel sizes, therefore, the number of voxels within each positive region is a poor indicator of the absolute physical size of the region. The size of a voxel plays an important role in discriminating between true positives and false positive based on region size, since the same number of image voxels describe different physical sizes depending on the resolution of the data. For instance, an image region of 100 voxels describe a larger physical region on a dataset with voxel size $0.5 \times 0.5 \times 1.00\,\text{mm}^3$ than is does on a dataset with voxel size $0.5 \times 0.5 \times 0.5\,\text{mm}^3$. In order to analyze positive regions in a unique manner across modalities and scanners, we define a *region*

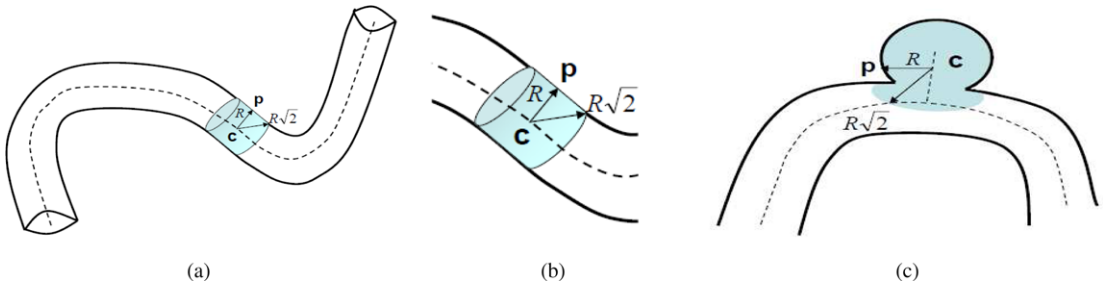


Fig. 2. Local neighborhood of surface point **p**. **c** is the point on a short branch closest to **p**. Most points **c** represent noise on the medial axis and sit close to the true medial axis of the normal vessels. The local neighborhood of **p** is build around **c** and is defined as the connected set of surface points whose Euclidean distance is within $R\sqrt{2}$ from **c** (a) **p** is a point on the surface of normal vessels and **c** is a noise point on the medial axis sitting close to the true medial axis of the region. (b) Detail of local neighborhood on healthy vessels. (c) **p** belongs to an aneurysm.

index as the product between the size of the region in voxels and the volume of the voxel. We effectively add the volume of all voxels on the surface of the positive region. We use the region index as an alternative to the surface area of the positive regions in order to avoid the triangulation of the surface. Under this definition, 100 voxels describe a region index of 25 on a dataset with voxel size $0.5 \times 0.5 \times 1.00$ mm^3. The same 100 voxels describe a region index of 12.5 on a dataset with voxel size $0.5 \times 0.5 \times 0.5$ mm^3. The region index gives an intuition of the physical size of a positive result independent of the resolution of the input data. True positives tend to have a larger region index than false positives and in this work we threshold positive results based on their region index. In Section 6, under Results, we show how detection and false positive statistics change according to the threshold value of the region index.

5. Clinical data

5.1. 3D-RA and CTA

The aneurysm detection method was tested on ten distinct 3D-RA and ten unrelated CTA patient-derived datasets. The twenty datasets contain twenty aneurysms, with one study showing no aneurysms and one study having two aneurysms. The aneurysms have diameters in the range 3.2–10.2 mm and lengths in the range 3.5–13 mm. Among the aneurysms, six are sidewall aneurysms (dilation of the artery in one direction perpendicular to the vessel axis), nine are bifurcation aneurysms (dilation at the bifurcation of arteries) and five are fusiform aneurysms (dilation of the artery in multiple directions more or less perpendicular to the vessel axis). All aneurysms were identified a priori and classified by two independent operators.

The 3D rotational angiography (3D-RA) data were acquired using a biplane flat-detector digital subtraction angiography system (Axiom Artis, Siemens Medical Solutions, Malvern, PA) at Tufts Medical Center, Department of Neurosurgery (Boston, MA). 3D-RA is a technique employed to visualize blood vessels in a bony or dense soft tissue environment. Contrast agent is injected through a catheter which is navigated from a percutaneous femoral arterial access into a carotid or vertebral artery (i.e. one of the vessels leading to the brain vasculature). Images acquired during the contrast agent are subtracted from images acquired pre-contrast. In the case of intracranial scanning, 3D-RA produces images with very high contrast between vasculature and the surrounding environment (Fig. 3a). In the current study, the size of each 3D-RA data volume is $256 \times 256 \times 229$, with 0.48 mm isotropic voxels.

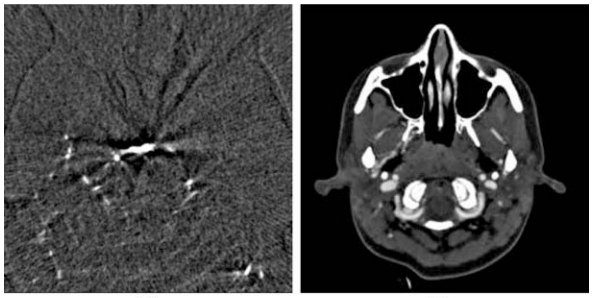


Fig. 3. (a) 3D-RA axial image (window 1000, level 200) displays high contrast between vasculature and surrounding tissue. (b) CTA axial image (window 700, level 250). The contrast agent injected during CTA imaging increases the image contrast between vessels and surrounding soft tissue, but lowers the contrast between vessels and bone.

To visualize blood vessels, CTA relies on 2D X-ray images acquired in the presence of an iodine-based contrast injected as an intravenous solution (Fig. 3b). Two scanners were used for the acquisition of the CTA datasets: definition (Siemens Medical Solutions, Malvern PA; voxel size $0.35 \times 0.35 \times 1$ mm) and LightSpeed Plus (GE Medical Systems, Schenectady NY; voxel size $0.40 \times 0.40 \times 1.25$ mm).

Although catheter-based 3D-RA imaging remains the gold standard in cerebral aneurysm imaging, CTA is a less-invasive modality with increasingly improving sensitivity and specificity, which is being more and more used for cerebrovascular imaging and aneurysm detection (Edlow et al., 2008).

5.2. Pre-processing

Prior to segmenting the vasculature, CTA data volumes were resampled to isotropic voxel size. Because of the high resolution of the data and high contrast between vasculature and surrounding tissue, vessel segmentation of 3D-RA data is a relatively simple task (Fig. 3a). CTA images have lower spatial resolution compared to 3D-RA and may show physical (partial volume, beam hardening) and patient-related artifacts (metal, motion effects) (Gupta et al., 2006). The contrast agent injected during CTA imaging increases the image contrast between vessels and surrounding soft tissue, but lowers the contrast between vessels and bone, making cerebral vessel segmentation more challenging (Fig. 3b). Furthermore, CTA data display venous contamination of the images (i.e. contrast agent reaching the venous system and precluding adequate visualization of arteries). In the case of CTA, the bone was removed from the images using a commercial 3D visualization and modeling system (Amira, Mercury Systems, Chelmsford, MA). Vessel segmentation was performed on all datasets using a combination of thresholding and region-growing techniques (Pham et al., 2000). The resulting segmented volumes were used as input to the aneurysm detection method.

5.3. Experimental validation of local neighborhoods

The detection method relies on the assumption that if the local neighborhood of a surface point on a normal vessel is determined as described in Section 4.5, it can be approximated by either a cylinder, in which case the medial axis is a line segment, or by an extruded parabola, in which case the medial axis is a parabola. The assumption was tested experimentally on the ten 3D-RA patient-derived datasets. Regression analysis was applied to each local neighborhood and points on the medial axis were fitted to both a line and a parabola. The smallest fitting error between the two determined if the local neighborhood was best approximated by a cylinder or by an extruded surface along a parabola.

Orthogonal linear regression (Ahn, 2004) was applied to minimize the perpendicular distances from the medial axis points to the fitting 3D line. As described in Ahn (2004), we fit a set $\{X_i\}_{i=1}^m$ of m points on the medial axis to a line described in parametric form by the equation $X_0 + u\mathbf{r} = 0$, where X_0 is a point on the line and the centroid of the medial axis points, $\mathbf{r}$ is a direction vector, $\|\mathbf{r}\| = 1$ and $u \in \mathbb{R}$. The orthogonal fitting is achieved by finding $\mathbf{r}$ which minimizes the square sum of the orthogonal distances from the points to the line

$$\min_{\mathbf{r}} \sum_{i=1}^{m} \|(X_i - X_0) \times \mathbf{r}\|^2.$$

Fig. 4 shows the histogram of line fitting errors. The horizontal axis represents corresponding root mean squared (RMS) errors defined as RMS $= \sqrt{\frac{1}{m}\sum_{i=1}^{m} \epsilon^2}$, where ϵ_i is the Euclidean distance from

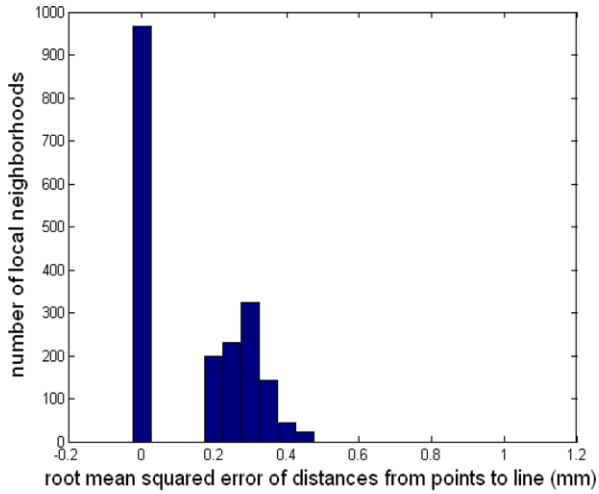


Fig. 4. Histogram of line fitting errors.

medial axis point i to the fitting line. The vertical axis shows the number of local neighborhoods which can be approximated by cylinders.

In the case of parabola fitting, first orthogonal regression was applied to fit the 3D medial axis points to an arbitrary plane described by the equation $(X - X_0)^T \cdot \mathbf{n} = 0$, where X is an arbitrary point on the plane, X_0 is a point on the plane and the centroid of the medial axis points, $\mathbf{n}$ is the normal to the plane and $\|\mathbf{n}\| = 1$ (Ahn, 2004). The orthogonal fitting is achieved by finding $\mathbf{n}$ which minimizes the square sum of the orthogonal distances from the points to the plane

$$\min_{\mathbf{n}} \sum_{i=1}^{m} \|(X_i - X_0)^T \cdot \mathbf{n}\|^2.$$

Fig. 5 shows the histogram for plane fitting errors. It can be seen that the medial axis points for each local neighborhood are very close to being coplanar.

The 3D points were then projected onto the fitting plane and represented as 2D points in a local coordinate system. The set of 2D points, $\{(x'_i, y'_i)\}_{i=1}^m$, were fitted to a 2D parabola described by equation $(y - k)^2 = 4a(x - h)$, where (h, k) is the vertex of the parabola and $a \in \mathbb{R}, a \neq 0$. In addition to minimizing the distances from points to parabola, we constrained the system such that the apex of the parabola was fixed to the center of the medial axis (point **c** from Fig. 2).

$$\min_a \sum_{i=1}^{m} \|(y_i - k)^2 - 4a(x_i - h)\|^2,$$

such that $c = (h, k)$.

The histogram for parabola fitting errors is shown in Fig. 6. On the horizontal axis are the corresponding RMS errors from the medial axis points to the fitting parabola. The vertical axis shows the number of local neighborhoods which can be approximated by extruded surfaces along a parabola.

Note that the maximum fitting errors in all three cases are smaller than the voxel size, which is $0.48 \times 0.48 \times 0.48$ mm^3. The local neighborhood analysis shows that it is reasonable to model small regions along normal vessels as cylinders and extruded parabolas. Deviations from such geometries are captured by the writhe number computations and provide a useful tool for finding aneurysms as abnormal vessel regions.

6. Results

All aneurysms were correctly identified by our detection method with 0.66 false positives per study on 3D-RA data and 5.36 false positives per study on CTA-derived data. These results were obtained as follows. As discussed in Section 4.7, we start by clustering voxels whose writhe number is non-zero and then computing the region index associated with each cluster. Suspect regions are taken as those whose region index exceeds a given threshold. The performance analysis in this paper is evaluated by varying this threshold and examining relevant statistics.

Specifically, for each threshold value, the following quantities were computed: number of true positives (TP), number of false positives (FP), number of false negatives (FN) and true positive fraction (TPF). The true positive fraction is defined as

$$\mathrm{TPF} = \frac{\mathrm{TP}}{\mathrm{TP} + \mathrm{FN}}.$$

The sensitivity of the method is measured in percentage and is computed as TPF $\times$ 100.

Tables 1 and 2 show how detection statistics change function of the region index threshold value applied on the detection results, for 3D-RA and CTA, respectively. It is apparent from the two tables that most false positive results have very small region indexes. The purpose when applying the region index threshold is to reduce the

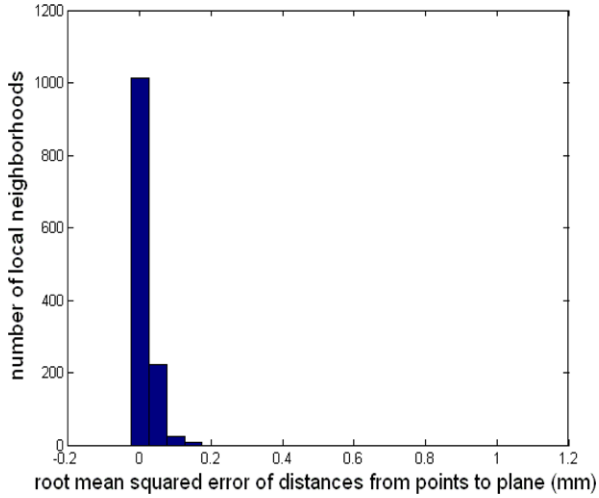


Fig. 5. Histogram of plane fitting errors.

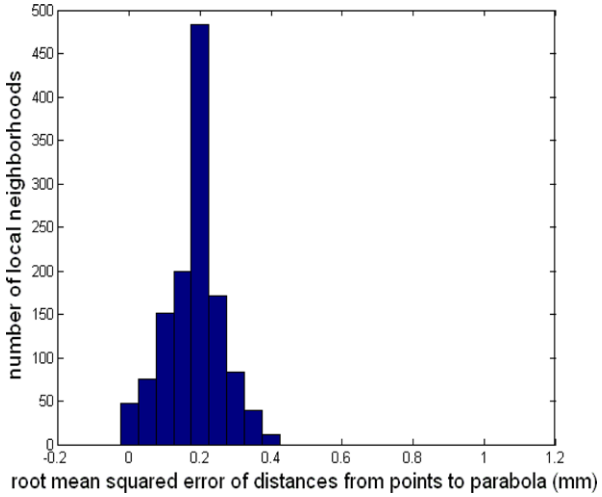


Fig. 6. Histogram of parabola fitting errors.

Table 1
Statistics for aneurysm detection on 3D-RA.

Threshold value (region index)	TPF (%/100)	FN (avrg per study)	FP (avrg per study)
0	1	0	3.66
5	1	0	1.33
7.5	1	0	1
10	1	0	0.66
12.5	0.87	0.11	0.44
15	0.50	0.33	0.22
17.5	0.35	0.33	0.22

Table 2
Statistics for aneurysm detection on CTA.

Threshold value (region index)	TPF (%/100)	FN (avrg per study)	FP (avrg per study)
0	1	0	28.80
5	1	0	5.36
7.5	0.90	0.10	3.27
10	0.81	0.18	2.27
12.5	0.81	0.18	1.54
15	0.81	0.18	1.36
17.5	0.63	0.36	1

FP value, while maintaining a TPF value of 1. TPF equals 1 when all aneurysms are detected.

The method detected all aneurysms and resulted in 3.66 false positives for 3D-RA data (Table 1) and 28.80 for CTA data (Table 2). These are detection results before any false positive reduction, which show that the detection specificity is much higher on 3D-RA data than on CTA. The first level of thresholding (with a region index of 5) reduces the CTA false positives from 28.80 to 5.36 and the 3D-RA positive results from 3.66 to 1.33, showing that most false positives are very small in size, especially for CTA data. The 3D-RA false positives can be further thresholding for a region index up to 10 which corresponds to 0.66 false positives per study.

To evaluate the performance of the proposed detection method, FROC analysis was applied as shown in Fig. 7. The horizontal axis indicates the average number of false positives (FP) per study, while the vertical axis indicates the true positive fraction (TPF), which is related to the sensitivity of the detection. Specifically, the FROC curves were determined by plotting TPF (second column from Tables 1 and 2) as a function of FP (fourth column from Tables 1 and 2) for both 3D-RA and CTA data. Fig. 7 shows how many false positive results are observed on average before one aneurysm is detected for 3D-RA (0.66 false positives) and CTA (5.36 false positives). The results correspond to thresholding positive results with a region index of 10 and 5 for 3D-RA and CTA, respectively.

The relationship between the writhe numbers and the size of the suspected regions is shown in Fig. 8. The horizontal axis holds the total writhe numbers for each positive result, computed as the sum of writhe numbers of all surface points on that positive result. On the vertical axis are the corresponding region indexes. True positives are shown as red stars and false positives are shown as blue stars. The analysis is done on the ten 3D-RA datasets. The figure shows that it is reasonable to use the size of the positive regions as a threshold value. It also suggests that both the size of the positive regions and the surface writhe number can be used to classify true positives vs. false positives using linear discriminant analysis. This is an interesting point and we plan to act on it in our future work which will incorporate classification on a larger one-modality database.

Figs. 9 and 10 show the visual results of the detection algorithm after thresholding positive results with region index smaller than 10. Red areas show positive results, while true aneurysms are indicated by a black arrow.

7. Discussions

The proposed aneurysm detection method was tested on twenty datasets from two imaging modalities, acquired with three different scanner models.

As shown by the FROC analysis, the detection algorithm performs very well on 3D-RA data and results in few false positive results (0.66 per study). 3D-RA images have high resolution and show high contrast between vasculature and surrounding tissue and simple segmentation techniques result in accurate segmented volumes. Segmentation is more challenging on CTA data which have lower resolution, more artifacts and show venous contamination.

There is a direct relationship between the quality of vessel segmentation and the accuracy of the detection method. Because this study focused on aneurysm detection, simple, readily available segmentation methods were used to preprocess the image data. However, particularly for CTA imaging, it is likely that better segmentation techniques (Hernandez and Frangi, 2007; Radaelli

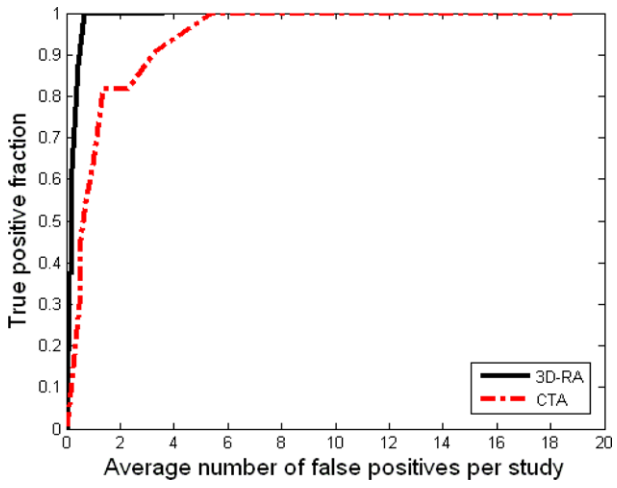


Fig. 7. FROC analysis of the aneurysm detection algorithm on 3D-RA and CTA data. The figure shows how many false positive results are observed on average before one aneurysm is detected for 3D-RA and CTA.

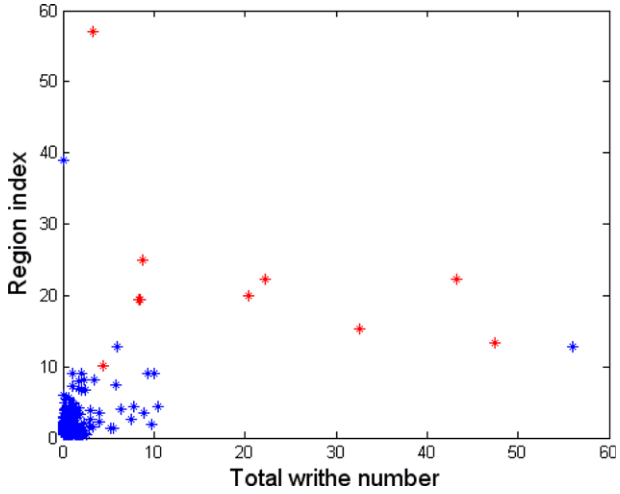


Fig. 8. Relationship between the writhe number and region index. The total writhe number of a positive region is computed as the sum of writhe numbers of all individual surface points. True positives are shown as red stars and false positives are shown as blue stars. The analysis is done on the ten 3D-RA datasets.

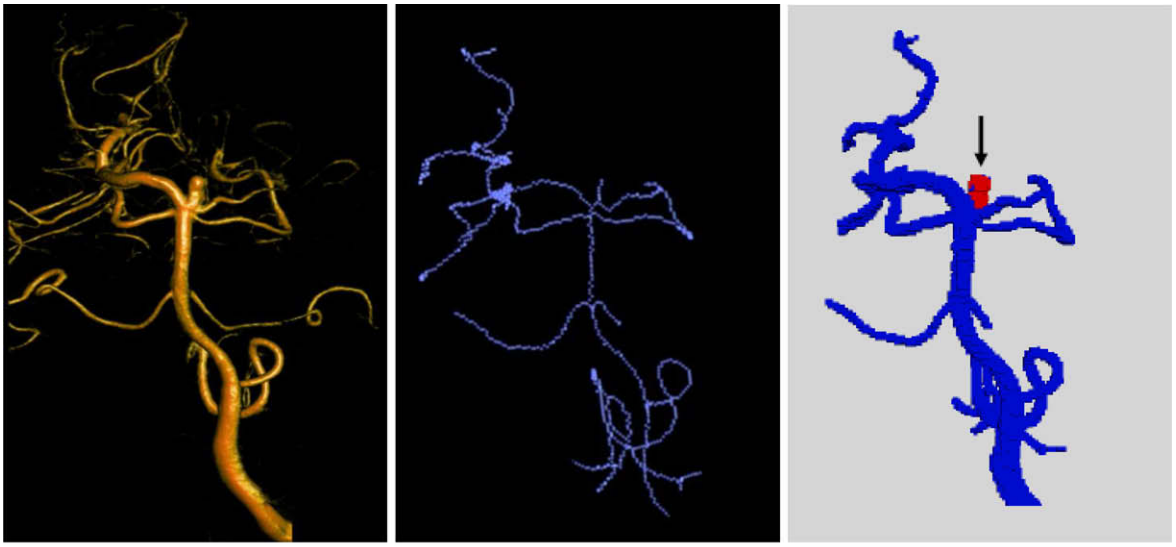


Fig. 9. Aneurysm detection results on one patient study. (a) Original 3D-rotational angiography. (b) Corresponding medial axis of the 3D-RA dataset. (c) Detection results. Positive results are colored in red. Black arrows point to true positives.

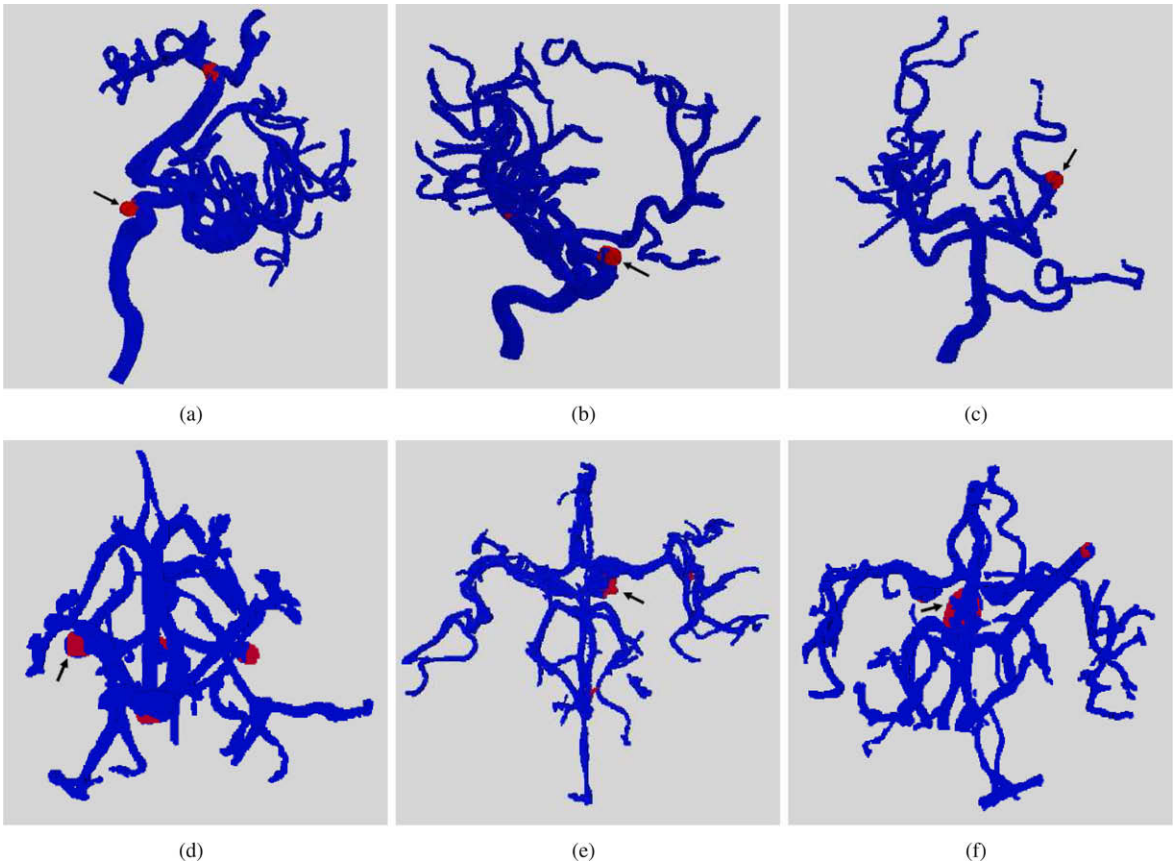


Fig. 10. Aneurysm detection on six patient-derived datasets. Results shown after thresholding positive results with a region index of 5. Positive results are colored in red. Black arrows point to true positives. Orientation is chosen for the best visualization of the aneurysms. (a–c) 3D-RA data. (d–f) CTA data.

and Peiro, 2009; Fridman et al., 2004) would improve the detection accuracy.

The clinical value of the algorithm depends on its performance on less-invasive CTA and MRA modalities. The current method is intended to be eventually generalized to include non-invasive cross-sectional imaging modalities and such studies will require an in-depth analysis of the characteristics, shortcomings and strengths of each imaging modality. The input modality will affect the choice of optimal segmentation algorithms and the effect of the segmentation performance on the detection results. While these complex issues were avoided by our use of 3D-RA data in this initial report, they will be the basis of future studies.

The presence of noise in the medial axis calculation, especially for narrow vessels (2–3 voxels in diameter) is the reason for a large

portion of the false positive results. The medial axis of the vessels is computed applying the method described by Bouix et al. (2005), which in tests on synthetic data showed a high percentage of voxel overlap between the computed medial axis and the ground truth medial axis. In regions where the computed medial axis did not overlap the ground truth medial axis, the average distance reported was half a voxel, with a maximum of one or two voxels distance, especially at the end points (Bouix et al., 2005). As it is expected the presence of noise influences the accuracy of the medial axis (Bouix et al., 2005). Some of the false positive detection results are located on peripheral vessels (2–3 voxels in diameter). While 3D-RA has excellent signal-to-noise ratio, the signal intensity is weaker in regions with small vessels compared to regions with main arteries and may influence the accuracy of the medial axis computation. At the same time, a half voxel discrepancy in medial axis computation has little impact when computing local neighborhoods in regions with wider vessels, but can result in incorrect local neighborhoods and false positive results in regions with much narrow vessels. For large, irregular aneurysms, the medial axis inside the aneurysm presents as a cluster of small branches rather than one branch, thus resulting in patches of positive results on the surface of the aneurysm as shown in Fig. 10f. The algorithm would benefit from an automated grouping of the positive results describing the same aneurysm. This would yield larger region indexes for true positives and a more discriminant false positive reduction. For future work we plan to study how smoothing of the medial axis affects false positive rates. There is a risk that smoothing of the medial axis might decrease the method sensitivity by removing small branches describing true positives.

The detection method correctly identified the five fusiform aneurysms from the test data. These are biological fusiform aneurysms which present as uneven dilatations in multiple directions perpendicular to the vessel axis. These aneurysms result in short branches on the vasculature centerline. The method is unlikely to detect true radially symmetric fusiform aneurysms defined as local dilatations of an artery and having perfectly circular cross-sections.

For future work, on a larger single modality database, we intend to improve false positive reduction using cross-validation for classification of the positive results taking into account features such as region index, estimated diameter, location on the vasculature and writhe number values.

Currently, the detection method requires an average of 2 min for a 3D-RA dataset and 8 min for CTA data on a desktop machine with Intel Duo Core@2.66GHz CPU and 2GB of RAM. This excludes segmentation time since we assume a segmented volume is given as input. On our particular data, we applied a combination of thresholding and region-growing segmentation techniques which take less than 1 min on both 3D-RA and CTA data. At the moment the code contains no optimization.

In terms of computational complexity, there is nothing inherently prohibitive in the proposed analysis, as all steps composing the detection method are computationally tractable. The local analysis work is highly parallelizable, and as such, is well suited to efficient implementation on advanced hardware such as multicore processors, FPGAs, ASICS, and GPUs. We are confident that code optimization and parallel programming will greatly decrease the required computation times and render the algorithm suitable for on-line use in clinical applications.

To assess the performance and utility of the aneurysm detection method in a clinical setting, we plan to perform a validation study, with and without computed-aided diagnostic systems assistance, to investigate the effect of our method on diagnostic accuracy. The detection of intracranial aneurysms is fraught by multiple confounding factors including the quality and age of the equipment available, the acquisition technique, patient cooperation, and clinician's expertise and state of alertness. Each of these factors is difficult to control or optimize on an ongoing basis. We believe an additional computational tool that would point the interpreting clinician to possible aneurysmal dilatations may be useful in improving diagnostic accuracy and reducing interpretation times.

8. Conclusion

A new method is presented for automated detection of intracranial aneurysms, which is based on the local 3D shape of the parent vessels. The writhe number is introduced as a new surface descriptor that can be used to distinguish between tubular and non-tubular regions along the vessels. The detection algorithm requires only a segmented volume of cerebral vasculature and is otherwise independent of the imaging modality. The method is tested on 3D-RA and CTA patient data. The robustness of the method is investigated analytically and validated experimentally. The method returns few false positive results and does not involve a complex false positive reduction scheme. In our experiments on patient-derived data, the sensitivity of the detection method is close to 100%.

Appendix A. Writhe number analysis

A.1. Writhe number of a cylinder

If $N(\mathbf{p})$ is a cylinder of radius R and length L and points $\mathbf{c}_0$ and $\mathbf{c}_1$ are the centers of the base and the top of the cylinder, respectively, then the medial axis of $N(\mathbf{p})$ is a line segment described by the parametric equation $m(t) = \mathbf{c}_0(1-t) + \mathbf{c}_1 t$, where $t \in [0,1]$. Without loss of generality, we assume that $\mathbf{c}_0$ is the origin of the local coordinate system, $\mathbf{c}_1$ lies on the $\mathbf{x}$ axis and the normal $\hat{\mathbf{n}}_\mathbf{p}$ at point $\mathbf{p}$ is parallel to the $\mathbf{y}$ axis (Fig. A.1). Points $\mathbf{p}_1, \mathbf{p}_2$ are chosen as discussed in Section 3.2.1.

Let $(\mathbf{p}_x, \mathbf{p}_y, \mathbf{p}_z)$ be the Cartesian coordinates of point $\mathbf{p}$. Point $\mathbf{p}_1$ sits on the circumference of a circle $C(\mathbf{p}_1)$ parallel to the base of $N(\mathbf{p})$. Let β be the angle between y axis and the vector from the origin of $C(\mathbf{p}_1)$ to point $\mathbf{p}_1$ (Fig. A.1). The same holds for point $\mathbf{p}_2$. For any pair of points $(\mathbf{p}_1, \mathbf{p}_2)$ the following are true:

$$
\begin{aligned}
&(\mathbf{p}_x, \mathbf{p}_y, \mathbf{p}_z) = \left(\frac{L}{2}, R, 0\right),\\
&(\mathbf{p}_{1x}, \mathbf{p}_{1y}, \mathbf{p}_{1z}) = (Lt, R\cos\beta, R\sin\beta), \quad t \in [0,1],\\
&(\mathbf{p}_{2x}, \mathbf{p}_{2y}, \mathbf{p}_{2z}) = (L(1-t), R\cos\beta, R\sin\beta), \quad t \in [0,1],\\
&(\mathbf{p}_1 - \mathbf{p}) = \left(Lt - \frac{L}{2}, R(\cos\beta - 1), R\sin\beta\right), \quad t \in [0,1],\\
&(\mathbf{p}_2 - \mathbf{p}) = \left(-Lt + \frac{L}{2}, R(\cos\beta - 1), R\sin\beta\right), \quad t \in [0,1],\\
&\hat{\mathbf{n}}_\mathbf{p} = (0,1,0),\\
&\hat{\mathbf{n}}_{\mathbf{p1}} = (0, \cos\beta, \sin\beta),\\
&\hat{\mathbf{n}}_{\mathbf{p2}} = (0, \cos\beta, \sin\beta),\\
&\hat{\mathbf{n}}_\mathbf{p} \times \hat{\mathbf{n}}_{\mathbf{p1}} = (\sin\beta, 0, 0),\\
&\hat{\mathbf{n}}_\mathbf{p} \times \hat{\mathbf{n}}_{\mathbf{p2}} = (\sin\beta, 0, 0),\\
&w(\mathbf{p}, \mathbf{p}_1) = (\mathbf{p}_1 - \mathbf{p}) \cdot (\hat{\mathbf{n}}_\mathbf{p} \times \hat{\mathbf{n}}_{\mathbf{p1}}) = \left(Lt - \frac{L}{2}\right)\sin\beta,\\
&w(\mathbf{p}, \mathbf{p}_2) = (\mathbf{p}_2 - \mathbf{p}) \cdot (\hat{\mathbf{n}}_\mathbf{p} \times \hat{\mathbf{n}}_{\mathbf{p2}}) = -\left(Lt - \frac{L}{2}\right)\sin\beta,\\
&w(\mathbf{p}, \mathbf{p}_1) = -w(\mathbf{p}, \mathbf{p}_2).
\end{aligned}
$$

A.2. Writhe number of an extruded surface along a parabola

An arbitrary parabola H, with the apex in the origin of the coordinate system, is defined by the parametric equations

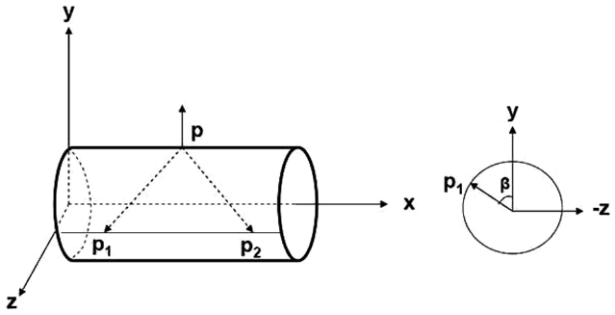


Fig. A.1. Computing the writhe number of a cylinder.

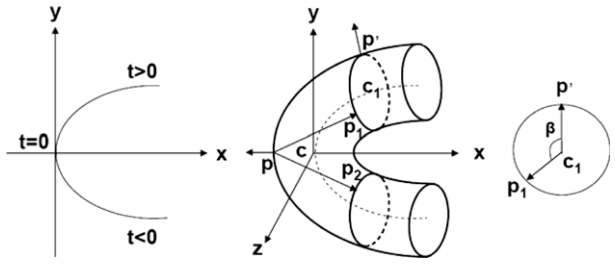


Fig. A.2. Computing the writhe number of an extruded parabola.

$x = at^2, y = 2at, t \in \mathbb{R}$. A point h on H has coordinates $(at^2, 2at)$ and the tangent to H at h is given by equation $ty = x + at^2$.

Given a surface point $\mathbf{p}$, let $N(\mathbf{p})$ be an extruded surface along H, having H as its medial axis. Point $\mathbf{p}$ lies on the circumference of a circle $C(\mathbf{p})$, with center $\mathbf{c}$ and perpendicular to H. Note that all the points on $C(\mathbf{p})$ have the same local neighborhood as $\mathbf{p}$ and implicitly the same writhe number. Without loss of generality, we assume that H lies in the xy plane, $\mathbf{c}$ is the apex of H and $\mathbf{p}$ is the apex of the largest parabola on the extruded surface, such that the normal $\hat{\mathbf{n}}_\mathbf{p}$ to the surface is parallel to the $\mathbf{x}$ axis (Fig. A.2). Points $\mathbf{p}_1, \mathbf{p}_2$ are chosen as discussed in Section 3.2.2.

Let $(\mathbf{p}_x, \mathbf{p}_y, \mathbf{p}_z)$ be the Cartesian coordinates of point $\mathbf{p}$ and $\mathbf{tp}$ be the tangent to the surface at point $\mathbf{p}$. Point $\mathbf{p}_1$ sits on the circumference of a circle $C(\mathbf{p}_1)$ with center $\mathbf{c}_1$ and perpendicular to H. $C(\mathbf{p}_1)$ intersects the largest parabola on the extruded surface in a point $\mathbf{p}'$, with normal $\hat{\mathbf{n}}'_\mathbf{p}$ to the surface. Let β be the angle between $\hat{\mathbf{n}}'_\mathbf{p}$ and the vector from $\mathbf{c}_1$ to point $\mathbf{p}_1$ (Fig. A.1). The same holds for point $\mathbf{p}_2$. For any pair of points $(\mathbf{p}_1, \mathbf{p}_2)$ the following are true:

$$(\mathbf{c}_x, \mathbf{c}_y, \mathbf{c}_z) = (0,0,0),$$
$$(\mathbf{c}_{1x}, \mathbf{c}_{1y}, \mathbf{c}_{1z}) = (at^2, 2at, 0), \quad t \in \mathbb{R},$$
$$(\mathbf{c}_{2x}, \mathbf{c}_{2y}, \mathbf{c}_{2z}) = (at^2, -2at, 0), \quad t \in \mathbb{R},$$
$$\hat{\mathbf{n}}_\mathbf{c} = (-1,0,0),$$
$$\hat{\mathbf{n}}_{\mathbf{c}1} = \left(-\frac{\frac{1}{t}}{\sqrt{1+\frac{1}{t^2}}}, \frac{1}{\sqrt{1+\frac{1}{t^2}}}, 0 \right), \quad t \in \mathbb{R},$$
$$\hat{\mathbf{n}}_{\mathbf{c}2} = \left(-\frac{\frac{1}{t}}{\sqrt{1+\frac{1}{t^2}}}, -\frac{1}{\sqrt{1+\frac{1}{t^2}}}, 0 \right), \quad t \in \mathbb{R},$$
$$\hat{\mathbf{t}}_{\mathbf{c}1} = \left(\frac{1}{\sqrt{1+\frac{1}{t^2}}}, \frac{\frac{1}{t}}{\sqrt{1+\frac{1}{t^2}}}, 0 \right), \quad t \in \mathbb{R},$$
$$\hat{\mathbf{t}}_{\mathbf{c}2} = \left(\frac{1}{\sqrt{1+\frac{1}{t^2}}}, -\frac{\frac{1}{t}}{\sqrt{1+\frac{1}{t^2}}}, 0 \right), \quad t \in \mathbb{R}.$$

The tuple $(\hat{\mathbf{t}}_{\mathbf{c}1}, \hat{\mathbf{n}}_{\mathbf{c}1}, \hat{\mathbf{t}}_{\mathbf{c}1} \times \hat{\mathbf{n}}_{\mathbf{c}1})$ is the basis of a 3D-RA orthogonal coordinate system local to $C(\mathbf{p}_1)$. Similarly, $(\hat{\mathbf{t}}_{\mathbf{c}2}, \hat{\mathbf{n}}_{\mathbf{c}2}, \hat{\mathbf{t}}_{\mathbf{c}2} \times \hat{\mathbf{n}}_{\mathbf{c}2})$ is the basis of an orthogonal coordinate system local to $C(\mathbf{p}_2)$. We will express $\mathbf{p}_1$ and $\mathbf{p}_2$ locally in terms of the new bases.

$$(\mathbf{p}_x, \mathbf{p}_y, \mathbf{p}_z) = (-R, 0, 0),$$
$$\mathbf{p}_{1x} = at^2 - \frac{\frac{R}{t}}{\sqrt{1+\frac{1}{t^2}}} \cos\beta, \quad t \in \mathbb{R},$$
$$\mathbf{p}_{1y} = 2at + \frac{R}{\sqrt{1+\frac{1}{t^2}}} \cos\beta, \quad t \in \mathbb{R},$$
$$\mathbf{p}_{1z} = R \sin\beta,$$
$$\mathbf{p}_{2x} = at^2 - \frac{\frac{R}{t}}{\sqrt{1+\frac{1}{t^2}}} \cos\beta, \quad t \in \mathbb{R},$$
$$\mathbf{p}_{2y} = -2at + \frac{R}{\sqrt{1+\frac{1}{t^2}}} \cos\beta, \quad t \in \mathbb{R},$$
$$\mathbf{p}_{2z} = R \sin\beta,$$
$$(\mathbf{p}_1 - \mathbf{p})_x = at^2 + R\left(1 - \frac{\frac{R}{t}}{\sqrt{1+\frac{1}{t^2}}} \cos\beta \right), \quad t \in \mathbb{R},$$
$$(\mathbf{p}_1 - \mathbf{p})_y = 2at - \frac{R}{\sqrt{1-\frac{1}{t^2}}} \cos\beta, \quad t \in \mathbb{R},$$
$$(\mathbf{p}_1 - \mathbf{p})_z = R \sin\beta,$$
$$(\mathbf{p}_2 - \mathbf{p})_x = at^2 + R\left(1 - \frac{\frac{R}{t}}{\sqrt{1+\frac{1}{t^2}}} \cos\beta \right), \quad t \in \mathbb{R},$$
$$(\mathbf{p}_2 - \mathbf{p})_y = -2at + \frac{R}{\sqrt{1+\frac{1}{t^2}}} \cos\beta, \quad t \in \mathbb{R},$$
$$(\mathbf{p}_2 - \mathbf{p})_z = R \sin\beta,$$
$$\hat{\mathbf{n}}_\mathbf{p} = (-1,0,0),$$
$$\hat{\mathbf{n}}_{\mathbf{c}1} = \left(-\frac{\frac{1}{t}}{\sqrt{1+\frac{1}{t^2}}}, \frac{1}{\sqrt{1+\frac{1}{t^2}}}, \sin\beta \right), \quad t \in \mathbb{R},$$
$$\hat{\mathbf{n}}_{\mathbf{c}2} = \left(-\frac{\frac{1}{t}}{\sqrt{1+\frac{1}{t^2}}}, -\frac{1}{\sqrt{1+\frac{1}{t^2}}}, \sin\beta \right), \quad t \in \mathbb{R},$$
$$\hat{\mathbf{n}}_\mathbf{p} \times \hat{\mathbf{n}}_{\mathbf{p}1} = \left(0, -\sin\beta, -\frac{1}{\sqrt{1+\frac{1}{t^2}}} \right), \quad t \in \mathbb{R},$$
$$\hat{\mathbf{n}}_\mathbf{p} \times \hat{\mathbf{n}}_{\mathbf{p}2} = \left(0, -\sin\beta, \frac{1}{\sqrt{1+\frac{1}{t^2}}} \right), \quad t \in \mathbb{R},$$
$$w(\mathbf{p}, \mathbf{p}_1) = (\mathbf{p}_1 - \mathbf{p}) \cdot (\hat{\mathbf{n}}_\mathbf{p} \times \hat{\mathbf{n}}_{\mathbf{p}1})$$
$$= -\left(2at - \frac{R\cos\beta}{\sqrt{1-\frac{1}{t^2}}} \right) \sin\beta - \frac{R}{\sqrt{1+\frac{1}{t^2}}} \sin\beta,$$
$$w(\mathbf{p}, \mathbf{p}_2) = (\mathbf{p}_2 - \mathbf{p}) \cdot (\hat{\mathbf{n}}_\mathbf{p} \times \hat{\mathbf{n}}_{\mathbf{p}2})$$
$$= -\left(-2at + \frac{R\cos\beta}{\sqrt{1-\frac{1}{t^2}}} \right) \sin\beta + \frac{R}{\sqrt{1+\frac{1}{t^2}}} \sin\beta,$$
$$w(\mathbf{p}, \mathbf{p}_1) = -w(\mathbf{p}, \mathbf{p}_2).$$

References

Agarwal, P., Edelsbrunner, H., Wang, Y., 2004. Computing the writhing number of a polygonal knot. Discrete and Computational Geometry 32 (1), 37–53.

Ahn, S.J., 2004. Least squares orthogonal distance fitting of curves and surfaces in space. Lecture Notes in Computer Science, vol. 3151. Springer, Berlin/Heidelberg.

Arimura, H., Li, Q., Korogi, Y., Hirai, T., Abe, H., Yamashita, Y., Katsuragawa, S., Ikeda, R., Doi, K., 2004. Automated computerized scheme for detection of unruptured intracranial aneurysms in three-dimensional magnetic resonance angiography. Academic Radiology 11 (10), 1093–1104.

Arimura, H., Li, Q., Korogi, Y., Hirai, T., Abe, H., Yamashita, Y., Katsuragawa, S., Ikeda, R., Doi, K., 2005. CAD scheme for detection of intracranial aneurysms in MRA based on 3D analysis of vessels skeletons and enhanced aneurysms. Proceedings of SPIE 5747, 967–974.

Arimura, H., Li, Q., Korogi, Y., Hirai, T., Katsuragawa, S., Yamashita, Y., Tsuchiya, K., Doi, K., 2006. Computerized detection of intracranial aneurysms for three-dimensional MR angiography: Feature extraction of small protrusions based on a shape-based difference image technique. Medical Physics 33 (2), 394–401.

Berger, M.A., Prior, C., 2006. The writhe of open and closed curves. Journal of Physics A: Mathematical and General 38 (26), 8321–8348.

Bouix, S., Siddiqi, K., Tannenbaum, A., 2005. Flux driven automatic centerline extraction. Medical Image Analysis 9 (3), 209–221.

Brisman, J.L., Song, J.K., Newell, D.W., 2006. Cerebral aneurysms. New England Journal of Medicine 355 (9), 928–939.

Edlow, J.A., Malek, A.M., Ogilvy, C.S., 2008. Aneurysmal subarachnoid hemorrhage: update for emergency physicians. Journal of Emergency Medicine 34 (3), 237–251.

Fridman, Y., Pizer, S.M., Aylward, S., Bullitt, E., 2004. Extracting branching tubular object geometry via cores. Medical Image Analysis 8 (3), 169–176.

Fuller, F.B., 1971. The writhing number of a space curve. Proceedings of the National Academy of Sciences of the USA 68 (4), 815–819.

Gupta, R., Jones, S.E., Mooyaart, E.A.Q., Pomerantz, S.R., 2006. Computed tomographic angiography in stroke imaging: fundamental principles, pathologic findings, and common pitfalls. Seminars in Ultrasound, CT, and MRI 27 (3), 221–2423.

Hargittai, I., Hargittai, M., 1994. Symmetry: A Unifying Concept. Shelter Publications.

Hernandez, M., Frangi, A.F., 2007. Non-parametric geodesic active regions: method and evaluation for cerebral aneurysms segmentation in 3dra and cta. Medical Image Analysis 11 (3), 224–241.

Hurdal, M.K., Gutierrez, J.B., Laing, C., Smith, D.A., 2008. Shape analysis for automated sulcal classification and parcellation of MRI data. Journal of Combinatorial Optimization 15 (3), 257–275.

Johnson, M.R., Good, C.D., Penny, W.D., Barnes, P.R., Scadding, J.W., 2001. Lesson of the week: playing the odds in clinical decision making: lessons from berry aneurysms undetected by magnetic resonance angiography. BMJ 322 (7298), 1347–1349.

Juvela, S., 2004. Treatment options of unruptured intracranial aneurysms. Stroke 35 (2), 372–374.

Kirbas, C., Quek, F.K.H., 2003. Vessel extraction techniques and algorithms: a survey. Proceedings of Third IEEE Symposium on BioInformatics and BioEngineering, 238–245.

Klenin, K., Langowski, J., 2000. Computation of writhe in modeling of supercoiled DNA. Biopolymers 54 (5), 307–317.

Kobashi, S., Kondo, K., Hata, Y., 2006. Computer-aided diagnosis of intracranial aneurysms in MRA images with case-based reasoning. IEICE Transactions on Information and Systems 89 (1), 340–350.

Luo, S., Zhong, Y., 2005. Extraction of brain vessels from magnetic resonance angiographic images: concise literature review, challenges, and proposals. Conference on Proceedings of IEEE Engineering in Medicine of Biological Society 2, 1422–1425.

Pham, D.L., Xu, C., Prince, J.L., 2000. Current methods in medical image segmentation. Annual Review of Biomedical Engineering 2, 315–337.

Radaelli, A.G., Peiro, J., 2009. On the segmentation of vascular geometries from medical images. Communications in Numerical Methods in Engineering, doi:10.1002/cnm.1290.

Rinkel, G.J., Djibuti, M., Algra, A., van Gijn, J., 1998. Prevalence and risk of rupture of intracranial aneurysms: a systematic review. Stroke 29 (1), 251–256.

Rooij, W.J.V., Sluzewski, M., 2006. Procedural morbidity and mortality of elective coil treatment of unruptured intracranial aneurysms. American Journal of Neuroradiology 27 (8), 1678–1680.

Rossetto, V., Maggs, A.C., 2003. Writhing geometry of open DNA. Journal of Chemical Physics 118, 9864–9874.

Suarez, J.I., Tarr, R.W., Selman, W.R., 2006. Aneurysmal subarachnoid hemorrhage. New England Journal of Medicine 354 (4), 387–396.

Uchiyama, Y., Ando, H., Yokoyama, R., Hara, T., Fujita, H., Iwama, T., 2005. Computer-aided diagnosis scheme for detection of unruptured intracranial aneurysms in MR angiography. Conference on Proceedings of IEEE Engineering in Medicine of Biological Society 3, 3031–3034.

Wardlaw, J.M., White, P.M., 2000. The detection and management of unruptured intracranial aneurysms. Brain 123 (2), 205–221.